Journal of Materials Chemistry C

ROYAL SOCIETY OF CHEMISTRY

REVIEW

View Article Online
View Journal | View Issue



Cite this: J. Mater. Chem. C, 2025, 13, 16

# High-performance, narrow-band green-emitting phosphors for white LEDs: recent advances and perspectives

Yujia Wan,[ab] Dongjie Liu,[a] Wei Yang,[ab] Yingsheng Wang,[ab] Min Zhang,[ab] Hongzhou Lian,*[a] Peipei Dang,*[a] Guogang Li *[c] and Jun Lin *[ab]

An ultrawide-color-gamut backlight is crucial for achieving ultrahigh definition and ultrahigh resolution liquid crystal displays (LCDs), where green-emitting phosphors with narrow spectral emission are the decisive factors. However, the key green-emitting phosphors currently used in light-emitting diode (LED) backlights, such as commercial β-SiAlON:$Eu^{2+}$, have the disadvantages of a wide emission band and large particles. In order to display more colorful and vivid photographs, there is an urgent need to accelerate the development of narrow-band green-emitting phosphors with independent intellectual property rights and high quantum efficiency. This article outlines the design of green-emitting phosphors and the improvement of their luminescent properties. From a design perspective, an optimal phosphor must consider the host material and the activator. The emission bands of $Tb^{3+}$, $Mn^{2+}$, $Ce^{3+}$ and $Eu^{2+}$ are usually located in the visible region, and the short luminescence decay time of $Eu^{2+}$/$Ce^{3+}$ makes it a potential activator for high-quality displays. In the exploration and selection of hosts for novel phosphors, approaches such as single-particle diagnosis, high-throughput density functional theory (DFT) calculations and mineral-inspired prototype evolution are commonly employed. Thermal stability and quantum efficiency (QE) are critical properties for phosphors, and various strategies to enhance these characteristics are discussed herein. Moreover, the color gamuts of various green-emitting phosphors are presented, highlighting their applications in green-emitting phosphor-based WLEDs used in LCD screens and projectors. These WLEDs display more vivid image quality than the conventional commercial WLEDs. Finally, the future outlook on exploring and developing green-emitting phosphors with enhanced performance is discussed.

Received 18th October 2024,
Accepted 21st November 2024

DOI: 10.1039/d4tc04457f

rsc.li/materials-c



## 1. Introduction

High-definition displays have become an essential part of daily life, serving as the display medium for devices such as televisions, computer displays and cellphones.[1,2] The backlight, which provides the light source for displaying images, determines the richness of the display colors. A variety of display technologies, including backlit liquid crystal displays (LCDs), organic light-emitting diodes (OLEDs), quantum dot LEDs (QLEDs) and micro-LEDs, with favorable luminescence performances have been widely studied and reported.[3–8] OLEDs, QLEDs, and micro-LEDs as novel approaches to achieve white light offer many advantages, such as high brightness, greater efficiency and low power consumption; however, these technologies still have several drawbacks.[9–13] The OLED has a high response time and large color gamut, but its short lifetime, poor thermal stability and high cost limit its further usage. Cd-based QDs as components of QLEDs are unstable in humid environments, and Cd is harmful to the environment.[14] The high cost of micro-LEDs hinder their further development in practical applications.[15–19] Phosphor-converted white LEDs (pc-WLEDs) are usually used to fabricate the backlight in LCDs due to their long lifetime, low energy consumption, and lower cost.[20–22] Hence, backlighting in LCDs is a reliable and mature technique that has been widely implemented and remains the subject of extensive research.[23–27]

The commercial backlight in LCDs contain pc-WLEDs fabricated by GaN blue chip, narrow-band green emitting β-SiAlON:$Eu^{2+}$ (β-SiAlON) and linear red emitting $K_2SiF_6$:$Mn^{4+}$ (KSF:$Mn^{4+}$) phosphors.[28] The level of backlighting used to display color can be measured by the color gamut, which is

[a] State Key Laboratory of Rare Earth Resource Utilization Changchun Institute of Applied Chemistry, Chinese Academy of Sciences Changchun, Jilin 130022, P. R. China. E-mail: ppdang@ciac.ac.cn, hzlian@ciac.ac.cn, jlin@ciac.ac.cn
[b] School of Applied Chemistry and Engineering University of Science and Technology of China Hefei, Anhui 230026, P. R. China
[c] Faculty of Materials Science and Chemistry China University of Geosciences Wuhan, Hubei 430074, P. R. China. E-mail: ggli@cug.edu.cn

the area of the triangle made up of the CIE coordinates of the red-, green-, and blue-emitting phosphors. The larger the triangle area, the more colors can be displayed, representing a high-quality display. In order to acquire more realistic display patterns, the color gamut should be further expanded. The blue and red emission coordinates formed by the GaN chip with the CIE coordinates (0.141, 0.042) and KSF:$Mn^{4+}$ phosphor with (0.692, 0.308) are very close to the blue and red edges of the gamut diagram, respectively. β-SiAlON, as a commercial phosphor, emits intense green light peaking at 538 nm with a FWHM of 48 nm and exhibits high internal quantum efficiency/absorption (IQE/Abs) of 91%/66%.[29] Moreover, β-SiAlON has good chemical and physical stability, and has demonstrated a long working life in practical applications. Xie's group developed a synthetic method for β-SiAlON that involved mechanical grinding and acid washing processes, which could efficiently improve the IQE to 79% even at small particle size of 3.13 μm.[30] This enhancement allows β-SiAlON to be used in mini-LEDs, providing a new solution for high-definition displays. However, owing to the bandwidth and peak position, the green coordinate calculated by the commercial β-SiAlON phosphor is (0.244, 0.633), which suggests there is room for improvement. Narrower green-emitting phosphors should be explored, whose color coordinate can be extended to the edge of the gamut diagram. More than that, the luminescence thermal stability of phosphors should be focused on, as it is important to maintain the original intensity at high temperature. Here, β-SiAlON suffers from poor luminescence thermal stability, and can only maintain 88% integrated intensity at 423 K, which should be further improved. It would be preferable to develop phosphors with zero thermal quenching. The brightness of the display will not decay after a long working time. Researchers have put forward a lot of methods to enhance the thermal stability, such as adding flux, cation substitution, and mineral-inspired evolution. Therefore, developing novel green phosphors with a narrow-band and good thermal stability is a key demand for backlit displays.[31,32]

In this review, we first discuss activators based on the classic visible emissions of $Mn^{2+}$, $Ce^{3+}$, $Eu^{2+}$, $Tb^{3+}$, and hosts based on three feasible approaches: single-particle diagnosis, high-throughput DFT calculations, and mineral-inspired prototype evolution. Next, we present multiple methods for modulating the luminescence and enhancing the luminescence thermal stability and QE. The color gamuts of green-emitting LEDs are further compared and the practicability examined for different kinds of application. Finally, we discuss the future development perspective of green-emitting phosphors, focusing especially on such phosphors with a small particle size with a high QE and thermal stability that could be used in mini-LEDs or micro-LEDs. We also recommend that theoretical study of the negative thermal quenching and abnormal luminescent situations should be further explored, and the theoretical selection of green-emitting phosphors with good performance should be established.

# 2. Design of green-emitting phosphors

## 2.1. Activator selection of green-emitting phosphors

A green-emitting phosphor should meet the requirements of a specific peak position (492–577 nm), and narrow-band emission with a FWHM of less than 60 nm. To expand the color gamut, the bandwidth should be narrower and the position should be better in the range of 520–530 nm. Based on these requirements, an excellent green-emitting phosphor should have a high luminescence efficiency, high thermal stability, and short luminescence decay time, which would contribute to its practical application in displays. From a design perspective, an inorganic phosphor includes the host and luminescence center, both of which can have a great influence on the luminescence performance. $Mn^{2+}$, $Ce^{3+}$, $Eu^{2+}$, and $Tb^{3+}$ are usually selected as the luminescence centers of green phosphors due to their emission bands being located in the visible region. Different host and intrinsic electronic structural properties will produce different luminescence, allowing green-emitting phosphors to be designed directionally.

The transition metal $Mn^{2+}$ shows the parity and spin-forbidden transition of d–d ($^4T_1 \rightarrow {}^6A_1$); however, the electronic transition will couple with part of the parity-allowed vibrations, making the emission band broad (Fig. 1a).[33,34] The outer d orbital is significantly affected by the local environment; therefore, the emission band mainly depends on the host structure.[35,36] $Mn^{2+}$ exhibits green emission after it is placed in a weak crystal field (tetrahedral coordination), and consequently, a lot of $Mn^{2+}$-doped green-emitting phosphors have been designed.[37,38] $Zn_4B_6O_{13}$ exhibits a tetrahedral coordinated lattice of $ZnO_4$ and $BO_4$ (Fig. 1b). $Mn^{2+}$ in $Zn_4B_6O_{13}$ emits green light, peaking at 540 nm with a FWHM of 33 nm (Fig. 1c) and shows near zero thermal quenching (ZTQ), maintaining a 103% initial intensity at 150 °C (Fig. 1d).[39] its symmetry space group $I\bar{4}3m$ and rigid structure contribute to its good thermal stability. However, $Mn^{2+}$-doped phosphors have some intrinsic drawbacks, owing to the spin-forbidden transition. Also, the excitation peak is narrow and the absorption is low, resulting in a low quantum efficiency. Moreover, $Mn^{2+}$-doped phosphors have a relatively long decay time of several ms, inducing a sticking image effect, which is not suitable for high-quality displays with a high refresh rate.

The rare earth ion $Tb^{3+}$ exhibits green emission due to an intrinsic electronic transition, which belongs to parity-forbidden transition of 4f–4f, where the 4f electron is shielded by the outer electron orbit of 5s; therefore, the emission spectrum is hardly affected by the local structure and $Tb^{3+}$shows an intrinsic emission.[40,41] The detailed emission transition of $Tb^{3+}$ is $^5D_4 \rightarrow {}^7F_J$ ($J$ = 3, 4, 5 and 6), which is presented as a line emission and is mainly located in the green region (Fig. 1e).[42,43] $Tb^{3+}$-doped green-emitting phosphors have been widely studied; for example, $NaYW_2O_8$:$Tb^{3+}$ has a main green emission peak at 545 nm and its main excitation peaks range from 200–400 nm, and so a heavy concentration of $Tb^{3+}$ can enhance the PL intensity (Fig. 1f and g). Moreover, $Tb^{3+}$

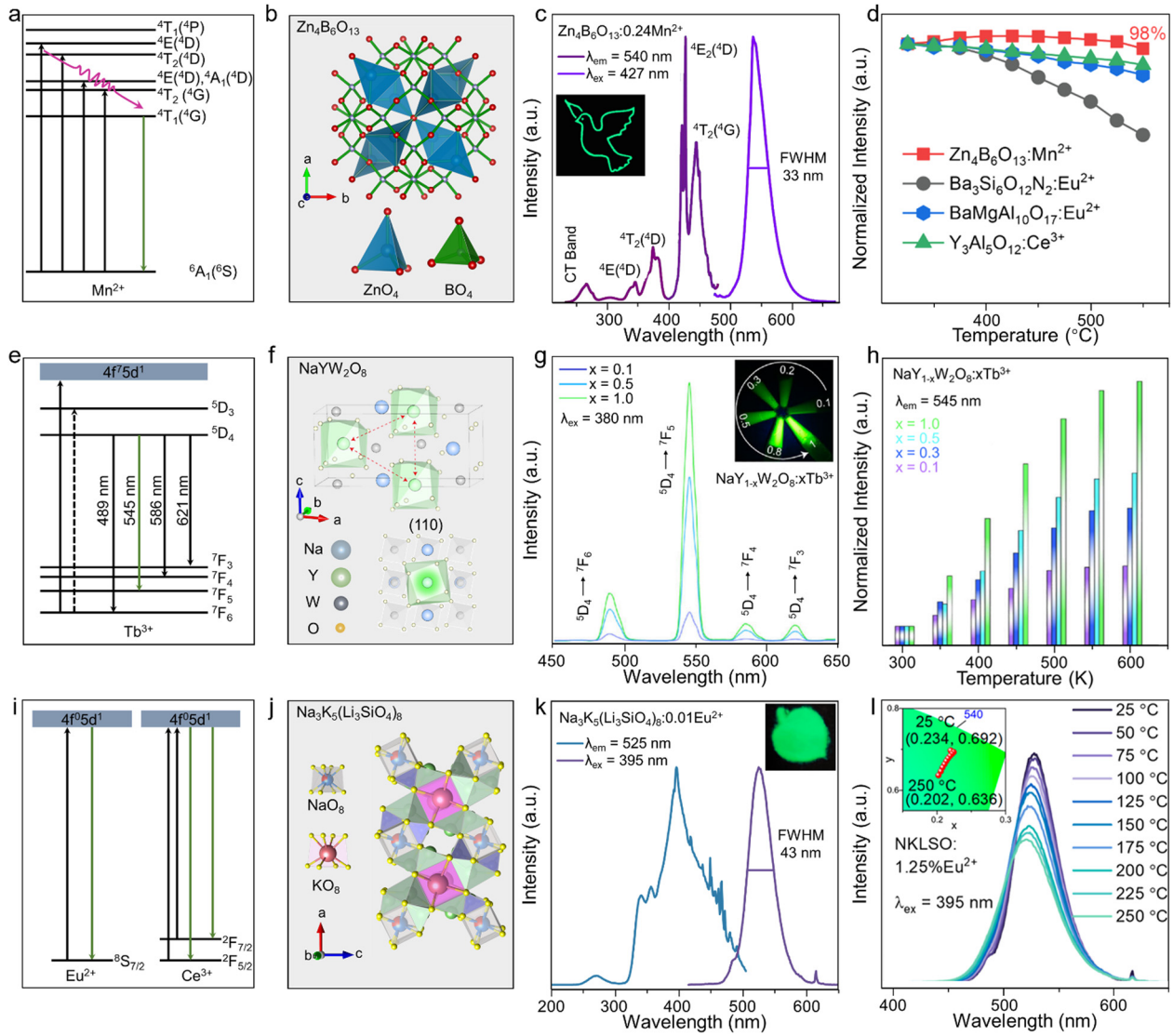


Fig. 1 (a) Energy level diagram of $Mn^{2+}$, where the purple line represents nonradiative transition. (b) Crystal structure of $Zn_4B_6O_{13}$ and the coordination polyhedra of $ZnO_4$ and $BO_4$, where the red balls represent the O atom. (c) PL and PLE spectra of $Zn_4B_6O_{13}$:$Mn^{2+}$. (d) Nearly ZTQ property of $Zn_4B_6O_{13}$:$Mn^{2+}$. (e) Energy level diagram of $Tb^{3+}$. (f) Crystal structure of $NaYW_2O_8$, where the blue, green, gray, and yellow balls represent Na, Y, W, and O, respectively. (g) PL spectra of $NaYW_2O_8$:$x$$Tb^{3+}$. (h) Anti-TQ property of $NaYW_2O_8$:$x$$Tb^{3+}$. (i) Energy level diagrams of $Eu^{2+}$ and $Ce^{3+}$. (j) Crystal structure of $Na_3K_5(Li_3SiO_4)_8$ and the coordination polyhedra of $NaO_8$ and $KO_8$. (k) PL and PLE spectra of $Na_3K_5(Li_3SiO_4)_8$:$Eu^{2+}$. (l) TQ property of $Na_3K_5(Li_3SiO_4)_8$:$Eu^{2+}$. Reproduced with permission from ref. 36. Copyright 2021, Elsevier, ref. 40. Copyright 2023, Wiley and ref. 26. Copyright 2023, The American Chemical Society.

shows good thermal stability in $NaYW_2O_8$, and the PL intensity can reach the highest, as a 20-fold increase, under excitation at 412 nm (Fig. 1h).[44] However, due to the 4f–5d allowed transition of $Tb^{3+}$ under excitation, the intensity of the 4d–5d excitation band is stronger than the other 4f–4f forbidden transition.[45] The characteristic excitation band of $Tb^{3+}$ is located in the range from 200–300 nm induced by the 4f–5d allowed transition and becomes the main excitation band. It is obvious that $Tb^{3+}$ singly-activated phosphors are usually excited by n-UV light, while there are few $Tb^{3+}$-doped phosphors excited by blue light, which limits their display application. A conventional strategy to expand the excitation band and enhance the luminescence quantum efficiency is by adding sensitizers, such as $Ce^{3+}$, $Pr^{3+}$, and $Sm^{3+}$.[46–48] The energy transfer to $Tb^{3+}$ was achieved by utilizing the intense emission of $Ce^{3+}$ in $Ca_2GdHf_2Al_3O_{12}$, a green-emitting phosphor, leading to $Ca_2GdHf_2Al_3O_{12}$:$Tb^{3+}$,$Ce^{3+}$, which exhibited 543 nm emission with a high IQE/EQE of 83%/66%.[49] However, because of the 4f–4f forbidden transition in emission, the luminescence lifetime of $Tb^{3+}$ also reached a ms level, which is not conducive to high-definition displays. Due to the relatively low luminescence efficiency induced by f–f transition and the difficulty of exciting $Tb^{3+}$ by blue chips for $Tb^{3+}$-doped phosphors, their application has been hindered so far.

The rare earth ions $Eu^{2+}$ and $Ce^{3+}$ with 4f–5d parity-allowed transition have attracted extensive attention for tuning the

 

bandwidth from ten to hundreds of nanometers (Fig. 1i).[50–56] The outer sphere 5d orbital is more susceptible to the crystal field than the 4f orbital. Hence, the band shape and width of a phosphor can be adjusted through modifying its crystal field environment. Benefiting from the allowed optical transition of 4f–5d transition, the emission and excitation band of $Eu^{2+}$ are band-shape, which usually has a high luminous efficiency. However, $Ce^{3+}$ is not suitable as an activator for narrow-band emission phosphors, as the 4f ground state of $Ce^{3+}$ is split into two energy levels, which results in a relatively broad-band emission. The excitation of $Eu^{2+}$-doped phosphors is usually located in the n-UV region and the spectrum of that usually shows broad-band emission induced by the allowed 4f–5d transition; hence, the host of $Eu^{2+}$ should be carefully selected. For a promising $Eu^{2+}$ activator doped in a host, a high symmetry lattice and coordination number are more likely to achieve green emission. Indeed, the eight-coordinated cube and distorted cube usually show a cyan to green emission. A lot of $Eu^{2+}$-doped green-emitting phosphors have been developed with good performance. $Na_3K_5(Li_3SiO_4)_8$:$Eu^{2+}$ ($N_3K_5$:$Eu^{2+}$) emits intense green light peaking at 525 nm with an FWHM of 43 nm (Fig. 1j and k), and also shows a high thermal stability and IQE. Also, its integrated intensity could be maintained at 96% at 150 °C compared to the value at room temperature (Fig. 1l), while its IQE was enhanced to near 100% after adding $Al^{3+}$ as a charge compensator.[29] The PL decay time of $Eu^{2+}$ usually exhibits a ns-level decay, which is more suitable for displays with high refresh rates. However, Eu and Ce normally exist in the form $Eu^{3+}$ and $Ce^{4+}$, respectively, while $Eu^{2+}$ and $Ce^{3+}$ are usually reduced in the reducing gas at the sintering temperature. Furthermore, the synthesis conditions required for $Eu^{2+}$ and $Ce^{3+}$ are more complicated than for $Tb^{3+}$ and $Mn^{2+}$. Moreover, owing to the two 4f energy levels ($^2F_{2/7}$ and $^2F_{2/5}$) of $Ce^{3+}$, the emission of $Ce^{3+}$ always exhibits two peaks, which is broader than $Eu^{2+}$ emission alone.

### 2.2. Host selection of green-emitting phosphors

It is a tedious process to use the traditional artificial trial-and-error method to explore new phosphors, as this likely consume a lot of money, time, and effort. Moreover, the luminescent properties of new phosphors, such as the peak position and width, may not meet the actual needs, resulting in a slow exploration of specific green-emitting phosphors. To meet the specific wavelength requirements and achieve customized green phosphors, there are three feasible and faster ways: (1) single-particle diagnosis, (2) high-throughput density functional theory (DFT) calculations, and (3) mineral-inspired prototype evolution. These methods have been extensively investigated and used to explore novel phosphors (Fig. 2a).

The first method is the single-particle diagnosis approach. Same luminescent centers, such as $Eu^{2+}$ and $Ce^{3+}$, may have varied emissions after doping into different hosts. Powder samples are usually synthesized as a mixed phase with different luminescence properties, making it difficult to observe the detailed luminescence and pure phase at the same time. The single-particle diagnosis approach can select the targeted luminescence after the powder is amplified to a single powder particle.[59,60] The particle sample can then be explored by single-crystal XRD and single-particle fluorescence spectroscopy. Finally, the powder phosphor can be synthesized after identifying its composition.[57] Xie's group explored a narrow-band green-emitting $Ba_2LiSi_7AlN_{12}$:$Eu^{2+}$ phosphor by single-particle diagnosis, and reported the particle emits green light under UV light, as shown in Fig. 2b and c. $Ba_2LiSi_7AlN_{12}$:$Eu^{2+}$ showed green luminescence peaking at 515 nm with a FWHM of 61 nm due to the symmetric lattice being occupied by $Eu^{2+}$ (Fig. 2d and e).[61]

Theoretical methods have also been identified as a highly efficient approach for developing new phosphors with specified optical properties, which also require less time than elaborate trial-and-error processes.[62–64] High-throughput DFT calculations are usually considered as a practical method for selecting targeted phosphors. Rami *et al.* proposed descriptors related to the emission energy position and bandwidth of $Eu^{2+}$-doped phosphors. Since the emission spectrum of $Eu^{2+}$ mainly depends on the 4f–5d transition process and is greatly affected by the 5d orbits, the (anti) bonding interaction between $Eu^{2+}$ and the ligands in 5d excited orbitals is proportional to the excited-state distortion. A group of phosphors $SrMg_3SiN_4$:$Eu^{2+}$ (SMS), $BaMg_3SiN_4$:$Eu^{2+}$ (BMS), $SrLiAl_3N_4$:$Eu^{2+}$ (SLA), $CaLiAl_3N_4$:$Eu^{2+}$ (CLA), $SrAl_2Li_2O_2N_2$:$Eu^{2+}$ (SALON), and $SrLi_2Be_4N_6$:$Eu^{2+}$ (SLBO) with similar structures were considered to construct an experimental law. By using the bandwidth as a function of the covalency coefficient $\alpha^2$ of the acceptor Eu 5d MO in the emission process, a linear relation could be fitted by the research between the experimental emission peak and the computed absorption energy maximum of the band (Fig. 2f and g). Based on the above analysis, high-level wavefunction-based *ab initio* quantum chemistry combined with time-dependent density functional theory (TD-DFT) and an excited-state dynamics (ESD) approach were used to develop a protocol for predicting the emission energy position and bandwidth of $Eu^{2+}$-doped phosphors (Fig. 2h).[65] Moreover, the host of a narrow-band emission phosphor can be directly selected in the crystal structure database (Fig. 2i). First, specific optical properties should be determined, such as narrow-band, green emission and good thermal stability, and then a series of descriptors can be proposed, such as the host band gap, host band structure, and Debye temperature. Second, the specific descriptor values can be determined by comparing the experimental data. Then, the specific descriptor values of phosphors in the crystal structure database can be calculated and the phosphors suited to the target conditions can be selected. For example, the Debye temperature can be used to indicate the strength of the structure rigidity, using the following formulae:

$$\Theta = \frac{\hbar}{k}\left[6\pi^2 V^{\frac{1}{2}} N\right]^{\frac{1}{3}} \sqrt{\frac{B_H}{M}} f(\nu) \quad (1)$$

$$f(\nu) = \left\{ 3\left[ 2\left(\frac{2}{3}\frac{1+\nu}{1-2\nu}\right)^{3/2} + \left(\frac{1}{3}\frac{1+\nu}{1-\nu}\right)^{3/2} \right]^{-1} \right\}^{1/3} \quad (2)$$

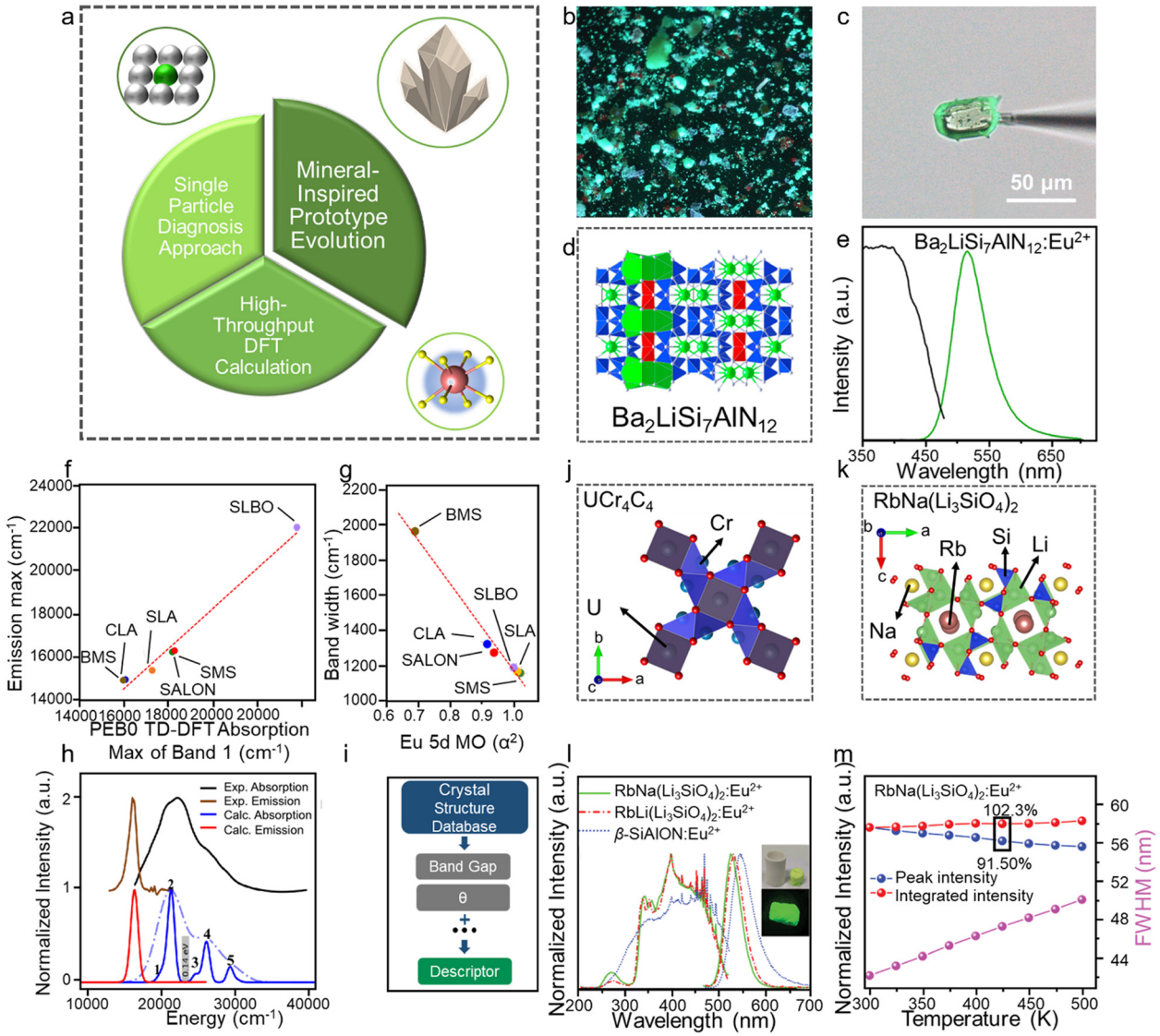


Fig. 2 (a) Schematic diagram of three approaches: single-particle diagnosis, mineral-inspired prototype evolution, and high-throughput DFT calculations. (b) Picture of the product synthesized by a mixture of Ba, Si, Al, Li, and Eu. (c) Green-emitting particle selected by the single-particle diagnosis approach. (d) Crystal structure of $Ba_2LiSi_7AlN_2$. (e) PL and PLE spectra of $Ba_2LiSi_7AlN_2:Eu^{2+}$. (f) Wave number of the experimental emission peak. (g) Experimental bandwidth as a function of the covalency coefficient $\alpha^2$ of the acceptor Eu 5d MO in the emission process for the SMS (green circle), BMS (brown circle), SLA (orange circle), CLA (blue circle), SALON (red circle), and SLBO (purple circle) materials. (h) SMS experimental (black), calculated TD-DFT/PBE0 absorption (blue, light blue) spectra, and experimental (brown), and TD-DFT/PBE0/ESD-calculated (red) emission spectra. (i) Simple flow diagram for selecting good-performing phosphors. (j) Crystal structure of $UCr_4C_4$. (k) Crystal structure of $RbNa(Li_3SiO_4)_2$. (l) PL and PLE spectra of $RbNa(Li_3SiO_4)_2:Eu^{2+}$. (m) Relative peak intensity and integrated intensity at different temperatures. Reproduced with permission from ref. 55. Copyright 2015, The American Chemical Society, ref. 57. Copyright 2022, American Chemical Society and ref. 58. Copyright 2019, Wiley.

where $\hbar$ is Plank's constant, $M$ is the molecular mass of the chemical formula, $k$ is the Boltzmann constant, $N$ is the number of atoms in one unit cell, $B_H$ is the bulk modulus of the crystal, $V$ is the volume of the unit cell, and $\nu$ is Poisson's ratio, which is related to the lateral deformation coefficient of the crystal.[66] The higher the Debye temperature, the stronger the rigidity. The commercial green-emitting β-SiAlON phosphor has relatively good luminescence thermal stability. The Debye temperature of phosphors can be obtained by both experimentation and calculation. When the Debye temperature of the phosphors is higher than that of β-SiAlON, it indicates the phosphor will have better thermal stability.

The final method to design new phosphors is by mineral-inspired prototype evolution based on specific mineral structure derivations, such as $UCr_4C_4$-type or garnet-type materials.[58,67] Through changing the atoms in a certain compound composition, the same or similar structure can be obtained, further leading to similar good luminescence properties. Taking the $UCr_4C_4$ type as an example, the composition $Me(A, B)_4X_4$ consists of alkali metal and alkaline earth metal

ions Me, and $[AX_4]$ and $[BX_4]$ tetrahedra connected with each other by common edges or vertices. Me ions are located in the framework to form the rigid structure with the density $\kappa = (AB/X) = 1$. $UCr_4C_4$-type materials have stable and rigid structures, as well as a cubic-like lattice. The high rigidity structure can reduce nonradiative transition, and the symmetric lattice sites can more easily emit narrow-band emission (Fig. 2j).[68–70] Due to the relative lower electronegativity and larger nephelauxetic effect of N in nitride than that of O in oxide,

$UCr_4C_4$-type nitride phosphors usually exhibit red emission, and oxide phosphors exhibit blue-to-green emission. Xia's group developed a series of $UCr_4C_4$-type oxide phosphors, and among them, the $RbNa(Li_3SiO_4)_2:Eu^{2+}$ (RN:$Eu^{2+}$) phosphor with a highly rigid structure emitted bright green light, peaking at 523 nm with a FWHM of 41 nm (Fig. 2k and l). The highly rigid structure and symmetry provide favorable conditions for good PL thermal stability, allowing RN:$Eu^{2+}$ to maintain a 102% integrated PL intensity at 152 °C (Fig. 2m).[71] The single-particle diagnosis approach can simplify the pure-phase process and reduce the synthesis time; however, this approach requires more sophisticated detected instruments for characterization, such as single-crystal XRD and single-particle fluorescence spectroscopy systems. Meanwhile, the high-throughput DFT calculation approach can greatly reduce the time compared to trial-and-error synthesis; although a lot of time is needed for building computational models and advanced computers for the calculations. Compare to these, mineral-inspired prototype evolution has emerged as a simple and time-saving way to explore new green-emitting phosphors, and can allow the directional design and synthesis of target phosphors by certain mineral prototypes. Among the many mineral prototypes, $UCr_4C_4$-type phosphors with excellent luminescence properties have received wide attention from researchers, and several green-emitting phosphors have been developed, as shown in Table 1. $UCr_4C_4$-type oxide phosphors usually exhibit narrow-band green emission peaking around 525 nm with a FWHM of less than 50 nm. Benefit from their high structural density and rigidity, $UCr_4C_4$-type phosphors have excellent PL thermal stability, and all of them can maintain a >95% integrated PL intensity at 150 °C. Based on the 4f–5d optically allowed transition of $Eu^{2+}$, their IQEs are relatively higher than that of normal green-emitting phosphors, whereas their EQEs need to be improved due to their low absorption. Additionally, the microcosmic mechanism of how the rigid structure affects the luminescence has been deeply studied. Ning's group combined first-principles calculations and the experimental data on $RbNa(Li_3SiO_4)_2$, and concluded that the emission band shape is basically controlled by electron–phonon coupling in $RbNa(Li_3SiO_4)_2$. They also provided insights on the emission bandwidth, stating that due to the high rigidity of the host, the structural strain caused by electron transition is well distributed. Hence the structural relaxation is weakened, further limiting the emission band broadening.[72] The enhancement of $UCr_4C_4$-type green-emitting phosphors should focus then on absorption enhancement. Table 1 lists a series of $UCr_4C_4$-type oxide green-emitting phosphors and their good luminescence properties.[71,73–76]

Although there are many green-emitting phosphors with good luminescence properties, there are still many aspects that should be improved for commercial LEDs. An excellent green-emitting phosphor for use in displays should be able to expand the color gamut as much as possible, as well as showing good thermal and chemical stability, a high quantum efficiency, and a facile synthesis. Hence, this provides inspiration to develop high-quality green-emitting phosphors for use in displays, with a special focus on three aspects: (1) color gamut, including the peak position, FWHM, and color purity; (2) stability, including thermal stability and other stability aspects under different working conditions, such as high humidity, long usage time, and high work current, and (3) high quantum efficiency.

### 2.3. Luminescence modulation

As mentioned above, the key point of the color gamut in displays is that the CIE color coordinate of green-emitting phosphors should be close to the edge of the gamut diagram. The color coordinate of phosphors depends on the peak position and FWHM of the emission spectrum. The peak position should range from 520–530 nm and the FWHM should be narrower than 50 nm. The selective conditions of green emission with different activators ($Tb^{3+}$, $Mn^{2+}$, $Ce^{3+}$, and $Eu^{2+}$) have been discussed previously, but further developments for achieving luminescence modulation should be further explored.[77]

The cationic substitution strategy is a common method for luminescent modification, and involves adjusting the crystal field intensity of an activator by changing its local crystal structure. $BaBeSiON_2:Eu^{2+}$ exhibited a red-shift when substituting Be with Si in $BaSi_2O_2N_2:Eu^{2+}$, which emitted blue light (Fig. 3a). Every second $(SiON_3)^{7-}$ unit was replaced by one $(BeN_3)^{7-}$, resulting in the substitution of O by N and inducing an enhancement in the crystal field splitting. $BaBeSiON_2:Eu^{2+}$

Table 1 Photoluminescence properties of green-emitting $UCr_4C_4$-type oxide phosphors, including their peak position, FWHM, thermal stability, and QE

| | | | | Quantum efficiency | |
|---|---|---|---|---|---|
| Formula | Peak position (nm) | FWHM (nm) | Thermal stability (integrated intensity), °C | IQE (%) | EQE (%) |
| $RbNa(Li_3SiO_4)_2:Eu^{2+}$ | 523 | 41 | 102%@152 | 96 | 44 |
| $Na_3K_5(Li_3SiO_4)_8:Eu^{2+}$ | 525 | 43 | 96%@150 | 100 | 40 |
| $Rb_3Na(Li_3SiO_4)_4:Eu^{2+}$ | 527 | 42 | 102%@150 | 85 | 40 |
| $NaK_2Li(Li_3SiO_4)_4:Eu^{2+}$ | 528 | 44 | 97%@150 | 81 | 51 |
| $RbLi(Li_3SiO_4)_2:Eu^{2+}$ | 530 | 42 | 103%@150 | 80 | 29 |
| $CsK_2Na(Li_3SiO_4)_4:Eu^{2+}$ | 531 | 46 | 96.3%@150 | 94 | 16 |

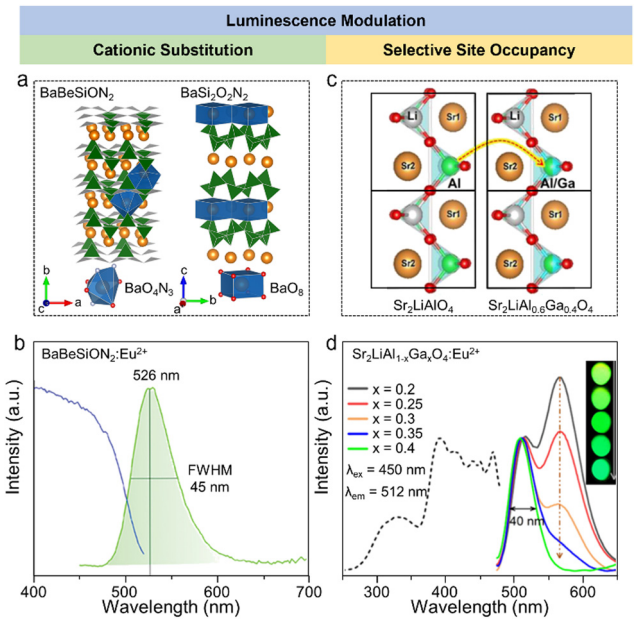


Fig. 3 (a) Crystal structures of $BaBeSiON_2$ and $BaSi_2O_2N_2$, and the coordination polyhedra of $BaO_4N_3$ and $BaO_8$ in $BaBeSiON_2$ and $BaSi_2O_2N_2$, respectively. (b) PL and PLE spectra of $BaBeSiON_2$:$Eu^{2+}$. (c) Variation diagram going from $Sr_2LiAlO_4$ to $Sr_2LiAl_{0.6}Ga_{0.4}O_4$. (d) PLE and PL spectra of $Sr_2LiAl_{1-x}Ga_xO_4$:$Eu^{2+}$ ($x$ = 0.2, 0.25, 0.3, 0.35, and 0.4). Reproduced with permission from ref. 73. Copyright 2024, Wiley and ref. 74. Copyright 2021, Wiley.

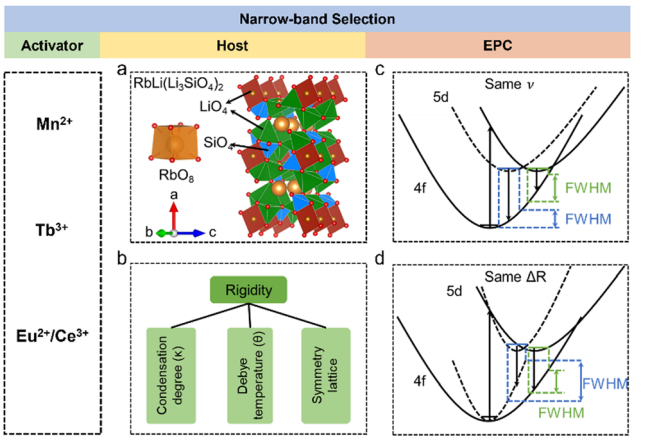


Fig. 4 (a) Crystal structures of $RbLi(Li_3SiO_4)_2$ and RbO8 coordination polyhedra. (b) Three criteria (condensation degree, Debye temperature, and symmetry lattice) for evaluating the structure rigidity. (c) Configuration coordinate diagram of $Eu^{2+}$ at same phonon frequency. (d) Configuration coordinate diagram of $Eu^{2+}$ at the same Stokes shift.

emitted green light peaking at 526 nm with a FWHM of 45 nm (Fig. 3b).[78] The other approach for luminescence modification is selective site occupancy, which changes the doped site or its coordination number by changing the local environment around activators. $Sr_2LiAl_{0.6}Ga_{0.4}O_4$:$Eu^{2+}$ exhibited green emission with a FWHM of 40 nm, and was obtained by substituting $Al^{3+}$ with $Ga^{3+}$ in $Sr_2LiAlO_4$:$Eu^{2+}$ with a green-yellow double peak emission (Fig. 3c). The introduction of $Ga^{3+}$ reduced the number of doped sites by compressing one of the luminescent sites and reducing the occupation, achieving a single peak green emission (Fig. 3d).[79] Another special example of luminescent modification was reported for $NaBaB_9O_{15}$:$Eu^{2+}$, where the activator $Eu^{2+}$ occupied an aliovalent $Na^+$ site rather than isovalent $Ba^2$, showing green emission peaking at 515 nm with a FWHM of 61 nm. The occupancy of $Eu^{2+}$ was regulated by the synthesis related to the energetic process, and the aliovalent $Na^+$ site preference occurred after an aging process at low temperature and was proved by DFT calculations. Due to the defects induced by the aliovalent substitution, this phosphor exhibited good thermal stability and the peak intensity was 110% at 500 K compared to at 300 K.[80]

### 2.4. Narrow-band selection

The condition of narrow-band emission should be further discussed. It can be research in three aspects: (1) the activator; (2) the host, and (3) the interaction between the activator and the host. The discussion on activators considered $Mn^{2+}$, $Tb^{3+}$, $Ce^{3+}$, and $Eu^{2+}$, which emit narrow-band green emission under specific conditions (Fig. 4 left), and the two latter cases are discussed in detail here. Host materials with high rigidity and high symmetry are more likely exhibit narrow-band emission. The rigid structure can reduce non-radiation relaxation by limiting the lattice vibration. The symmetry crystal lattice in the host can reduce the crystal field splitting, which favors the narrow-band emission (Fig. 4a). The rigidity of the structure can be selected based on many aspects (Fig. 4b), including the degree of condensation ($\kappa$), where a higher κ represents higher rigidity. The rigidity can be compared by comparing the value of $\kappa$, and the acknowledged highly rigid $UC_4C_4$-type has a high $\kappa$, where $\kappa$ = 1 (AB/X, as mentioned above). However, the connections in the structural framework are different to each other. Some are three-dimensional connections, which are relatively simple, while others are not, and thus it is difficult to compare their rigidity. The Debye temperature ($\theta$) was proposed as another way to compare rigidity, which can be obtained by theoretical calculations and by experiment, whereby high rigidity usually exhibits a high $\theta$.[81–83] Phosphors with a $\theta$ higher than that of commercial phosphor $Y_3Al_5O_{12}$ (YAG, $\theta$ = 726 K) are usually regarded as highly rigid materials.[66] Moreover, a lattice doped by an activator with high symmetry will more likely exhibit narrow-band emission due to the small lattice distortion. The interaction between the activator and the host materials is the interaction between the transition electron and the lattice vibration (phonon), which is also known as electron–phonon coupling (EPC). Intense EPC can induce non-radiative transition (where the transition electron releases energy as heat), which results in spectral broadening. The strength of EPC cannot be directly compared, but the equation and diagram are provided to aid discussing EPC. The Huang–Rhys factor ($S$) and Stokes shift ($\Delta R$) are fitted by a temperature-dependent relationship to compare with EPC, as shown in the following equations:

$$\Delta R = \sqrt{\frac{2hS}{h\nu}} \quad (3)$$

$$\mathrm{FWHM}^2 = 8\ln 2 S(h\nu)^2 \coth\left(\frac{h\nu}{2kT}\right) \quad (4)$$

$$\mathrm{FWHM} = 2\sqrt{\ln 2 \Delta R h\nu} \times \sqrt{\coth\frac{h\nu}{2kT}} \quad (5)$$

where $S$ is the Huang–Rhys factor, $h\nu$ is the vibrational phonon energy, $\nu$ is the phonon frequency, $k$ is the Boltzmann constant, and the $T$ is the temperature.

It is obvious that the FWHM is dependent on the $\Delta R$ or $S$, which is related to crystal structure relaxation and $\nu$, as shown in eqn (3). Moreover, a configuration coordinate diagram can be used to intuitively display the effect of phonons on electrons. Take the configuration coordinate diagram of $Eu^{2+}$ as an example, when the $\nu$ is the same (same parabolic shape) under different crystal structure relaxation (Fig. 4c), the smaller $\Delta R$ leads to a narrower FWHM, whereas when the $\Delta R$ is the same at different $\nu$, a smaller $\nu$ (parabola with large opening) leads to a narrower FWHM (Fig. 4d).

# 3. Performance enhancement of green-emitting phosphors

## 3.1. Thermal stability improvement

The other important property related to the rigidity and EPC of the host materials is the luminescence thermal stability. After a long working time, the heating effect of the phosphor can become a noteworthy problem, which should be further solved.[81] A phosphor with good thermal stability can maintain high brightness at high temperature, which should be further developed. A group of green-emitting phosphors, namely, $LaZnAl_{11}O_{19}:Mn^{2+}$ (LZAO:$Mn^{2+}$), $BaZn_{10}O_{17}:Mn^{2+}$ (BZAO:$Mn^{2+}$), $La_{0.827}Al_{11.9}O_{19.9}:Mn^{2+}$ (LAO:$Mn^{2+}$), $RbNa(Li_3SiO_4)_2:Eu^{2+}$ (RN:$Eu^{2+}$), $Na_3K_5(Li_3SiO_4)_8:Eu^{2+}$ ($N_3K_5$:$Eu^{2+}$), $Rb_3Na(Li_3SiO_4)_4:Eu^{2+}$ ($R_3N$:$Eu^{2+}$), $NaK_2Li(Li_3SiO_4)_4:Eu^{2+}$ ($NK_2L$:$Eu^{2+}$), $RbBaBP_2O_8:Tb^{3+}$ (RBBPO:$Tb^{3+}$). $BaY_4Si_5O_{17}:Tb^{3+},Ce^{3+}$ (BYSO:$Tb^{3+}$,$Ce^{3+}$), and $Ca_2GdHf_2Al_3O_{12}:Tb^{3+},Ce^{3+}$ (CGHAO:$Tb^{3+}$,$Ce^{3+}$) doped by $Mn^{2+}$, $Eu^{2+}$, and $Tb^{3+}$ were selected to compare their thermal stabilities and peak wavelengths (Fig. 5a). The region of the yellow area (peak position from 520–530 nm) crossing the orange area (relative integrated intensity

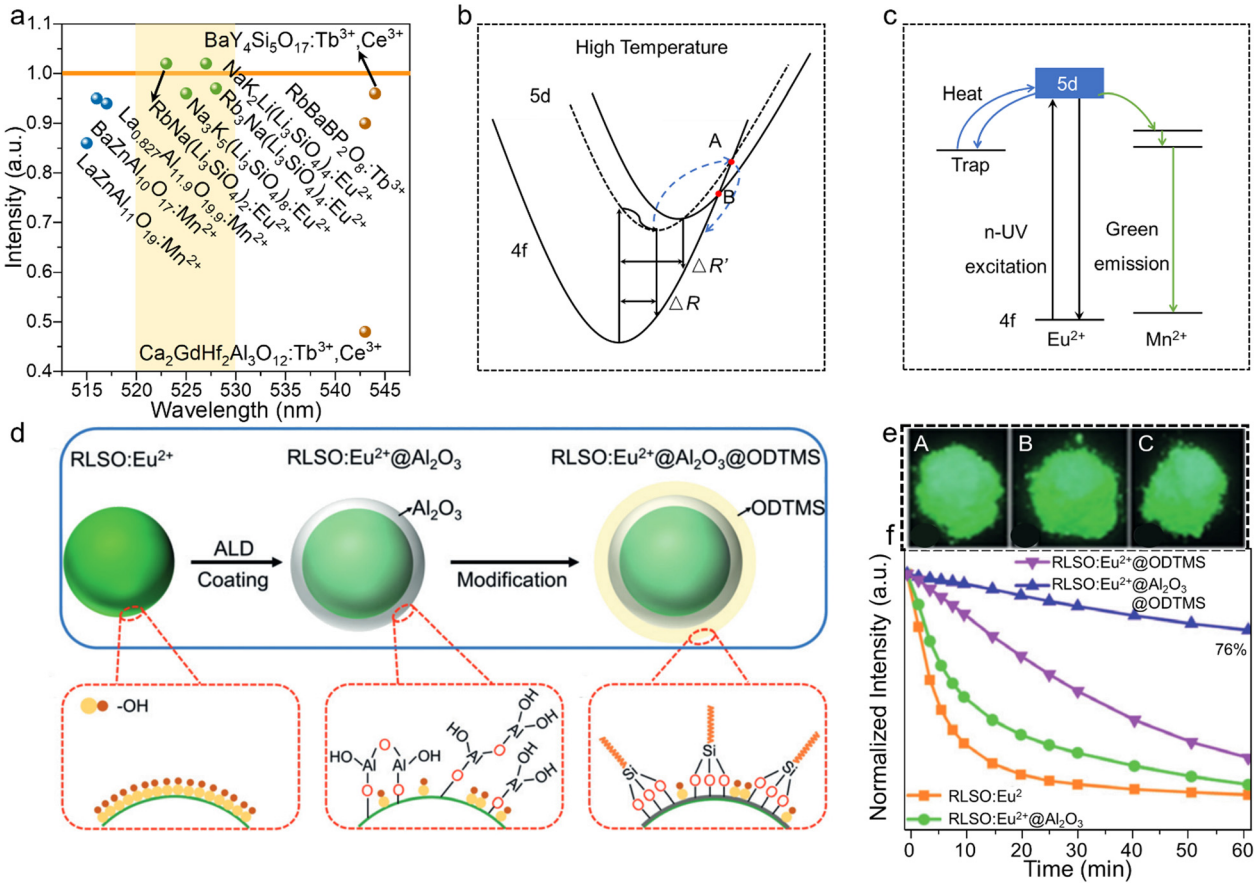


Fig. 5 (a) Wavelength (nm) and relative luminescence intensities of LZAO:$Mn^{2+}$, BZAO:$Mn^{2+}$, LAO:$Mn^{2+}$, RN:$Eu^{2+}$, $N_3K_5$:$Eu^{2+}$, $R_3N$:$Eu^{2+}$, $NK_2L$:$Eu^{2+}$, RBBPO:$Tb^{3+}$, BYSO:$Tb^{3+}$,$Ce^{3+}$, and CGHAO:$Tb^{3+}$,$Ce^{3+}$ at 150 °C compared to at 30 °C. (b) Configuration coordinate diagram of $Eu^{2+}$ at high temperature. (c) Energy level diagram for $Eu^{2+}$, $Mn^{2+}$, and the trap, and the electron transition process between them. (d) Process from RLSO:$Eu^{2+}$ to being covered by $Al_2O_3$ and the hydrophobic surface modification with ODTMS. (e) Photographs of RLSO:$Eu^{2+}$ (A), RLSO:$Eu^{2+}$@$Al_2O_3$ (B), and RLSO:$Eu^{2+}$@$Al_2O_3$@ODTMS (C). (f) Normalized intensities of RLSO:$Eu^{2+}$, RLSO:$Eu^{2+}$@$Al_2O_3$, and RLSO:$Eu^{2+}$@$Al_2O_3$@ODTMS after immersing in water for different times. Reproduced with permission from ref. 82. Copyright 2020, Wiley.

maintained at 100% at 150 °C) captures the green-emitting phosphors with an appropriate peak position and excellent thermal stability. The attenuation of the PL intensity generally comes from an increase in nonradiative transition and EPC with increasing temperature. Normally, a structure with high rigidity will exhibit good thermal stability, whereby the limitation of the lattice vibration can effectively reduce non-radiation induced by the heating effect. Taking the configuration coordinate diagram of $Eu^{2+}$ at high temperature as an example, the $\Delta R$ at high temperature was larger than that at room temperature, also indicating a larger FWHM at high temperature. Limiting the EPC of phosphors can effectively reduce the $\Delta R$ and FWHM (Fig. 5b). Selecting a highly rigid structure contributes to directionally selecting phosphors with good thermal stability, with the conditions for selecting structures with high rigidity discussed above.

The typical $UCr_4C_4$-type phosphors with high rigidity exhibited good thermal stability (Table 1), with all of them maintaining an over 95% integrated intensity at 150 °C. The other way to enhance the thermal stability is to construct a trap level. Here, part of the excited-state electrons are captured by the trap level in the transition, and then return to the ground state, emitting light.[84] Cation heterovalent substitution can induce vacancy or oxygen defects, which can store the energy and enhance the thermal stability. The cation for generating the defects can come from two sources: doped heterovalent activator ions and the cation of the host. $Na_{1.6}Al_{11}O_{17}$:$Eu^{2+}$,$Mn^{2+}$ induces oxygen vacancies by replacing $Eu^{2+}$ with $Na^+$, achieving anti-thermal quenching through releasing energy from the traps after heating (Fig. 5c). Moreover, the emission spectrum of that was found to fall within green light ($\lambda_{em}$ = 510 nm) with a FWHM of 27 nm and reached high IQE/EQE values of 81.8%/55.4%.[84,85] For practical application in daily life, except for the heating effect that occurs during the operation, other situations should also receive more attention, such as the high humidity and high working current. For instance, $UCr_4C_4$-type phosphors with excellent luminescent properties suffer from weak humid stability due to the existence of alkali metal ions Li, Na, K, Rb, Cs, and so a key challenge for their practical application is to focus on enhancing their humidity stability. $RbLi(Li_3SiO_4)_2$:$Eu^{2+}$ (RLSO:$Eu^{2+}$) emits green light with excellent thermal stability (103%@150 °C); however, it can easily form RbOH, LiOH, and $Li_2SiO_3$ after reacting with water. Xia's group coated amorphous $Al_2O_3$ and hydrophobic octadecyltrimethoxysilane (ODTMS) (Fig. 5d) on the surface to enhance the moisture-resistant property of $RbLi(Li_3SiO_4)_2$:$Eu^{2+}$, and found the intensity could be maintained at 76% and it showed intense green light after being submerged for 1 h (Fig. 5e and f).[86] Laser-driven solid-state white light sources represent a likely future research hotspot due to their high brightness, and small size, *etc.*[87] However, the luminescence saturation induced by high power hinders the use of normal phosphors, and so phosphors with a high-power-resistant property should be further developed.[88,89] Green-emitting ceramics to be used for laser diodes (LDs) should have excellent thermal stability and thermal conductivity, while the commercial green-emitting ceramic $Lu_3Al_5O_{12}$:$Ce^{3+}$ (LuAG:$Ce^{3+}$) has been developed as a phosphor-in-silica glass with an enhanced high-power-resistant property.[90,91] There have been few studies on other green-emitting ceramics to date, and so these should be further explored. The color purity is a comprehensive index to evaluate the spectrum width, which indicates the vividness of the color.

The narrower the spectrum of a phosphor is, the closer to the main wavelength it is, and the higher the color purity will be. Hence, the color purity should be calculated from the CIE chromaticity coordinates of the narrow-band green-emitting phosphors. The emission band of the phosphors will broaden at high temperature, and so the FWHM and peak position at different temperatures can be compared to discuss the strength of nonradiative relaxation. The color drift is only compared using the CIE color coordinates; however, a relationship between the peak broadening and the emitting color is rarely noticed. The change of color purity with increasing temperature can be discussed in depth to show the effect of temperature on the luminescence color and color draft in practical applications.

### 3.2. Quantum efficiency enhancement

Quantum efficiency (QE) is a vital factor for the commercialization of phosphors, as phosphors with a high quantum efficiency can reduce the energy consumption and save costs.[92] Research on improving the QE has been widely performed, and many methods have been tried to improve the QE, such as (1) adding flux, (2) constructing an energy transfer mechanism, (3) substituting the cation, and (4) adding a charge compensator. The addition of fluxes ($H_3BO_3$, $BaF_2$, and $Li_2CO_3$, *etc.*) can help to melt the raw material and reduce the sintering temperature.[93–95] Samples at lower sintering temperatures have less defects and increases crystallinity, which can help to reduce the energy loss and enhance the QE. Moreover, the addition of fluxes may remove the impurities situation during the sintering process though vaporization of the fluxes. It was found that after adding the flux, $Lu_3Al_5O_{12}$:$Ce^{3+}$ displayed an effectively enhanced intensity, as shown in Fig. 6a.[96] The addition of a single activator in the host may exhibit weak luminescence and a low QE, and so an energy transfer mechanism though the overlapping spectra was designed to enhance the QE. Adding a sensitizer with broad-band absorption is an efficient method to achieve energy transfer, which can stimulate the luminescence of the activator by enabling the transfer of excitation energy toward excitation of the activator. Co-doping $Ce^{3+}$ and $Tb^{3+}$ in the $Ca_2YZr_2(AlO_4)_3$ (CYZA) green-emitting phosphor resulted in a higher IQE of 56% compared to that of 26% for $Tb^{3+}$-doped CYZA due to the energy transfer between the excitation band of $Tb^{3+}$ and emission band of $Ce^{3+}$ (Fig. 6b).[97] The enhancement of the QE by cation substitution can be mechanistically explained by the effect of the crystal field. Changes in the crystal field can directly influence its strength, symmetry, and coordination number, and these changes can affect the energy level structure of the activators and enhance the QE. By replacing the $Rb^+$ in $Rb_4(Li_3SiO_4)_4$:$Eu^{2+}$ ($R_4LSO$:$Eu^{2+}$) by $Na^+$, $Rb_3Na(Li_3SiO_4)_4$:$Eu^{2+}$ ($R_3NLSO$:$Eu^{2+}$) was formed, resulting in an improvement of the IQE/EQE values

 

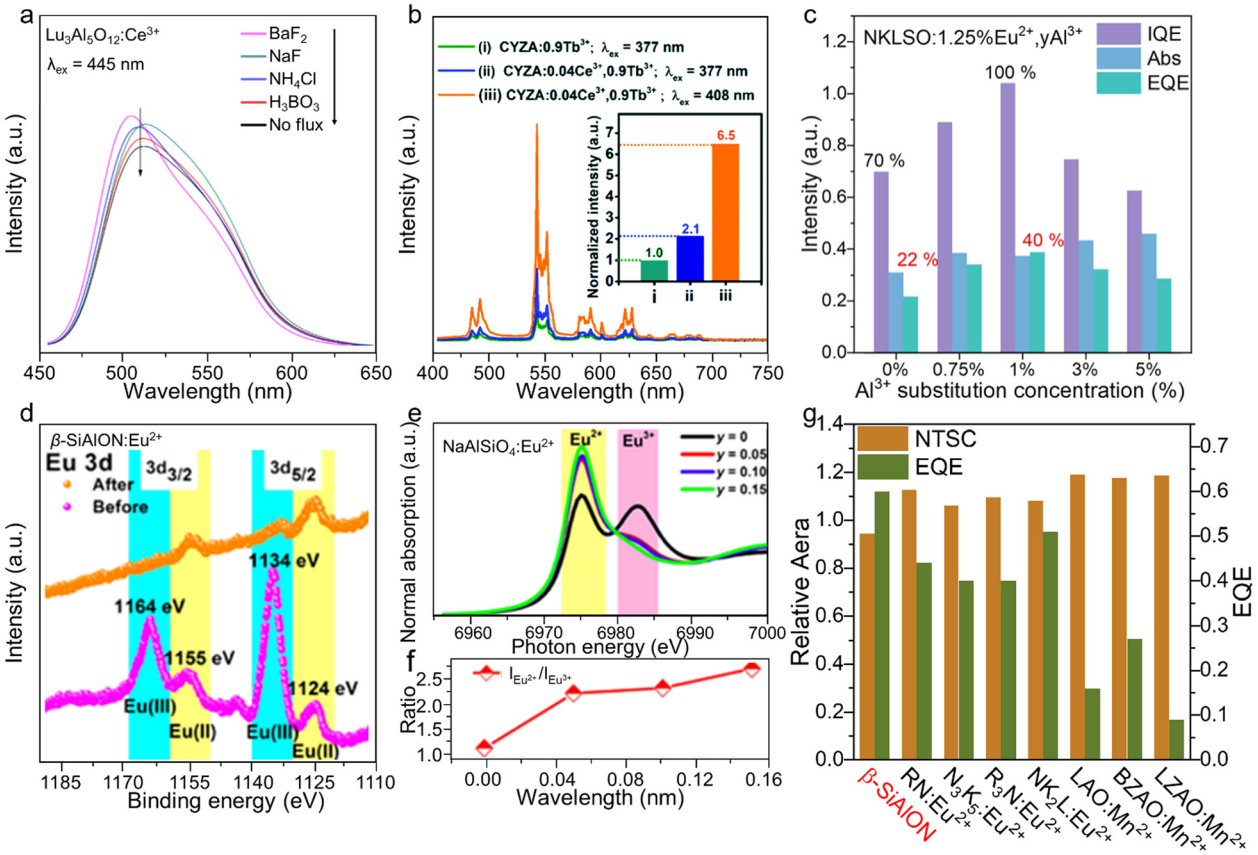


Fig. 6 (a) PL spectra of $Lu_3Al_5O_{12}:Ce^{3+}$ with different fluxes. (b) PL spectra of CYZA:$Tb^{3+}$, CYZA:$Tb^{3+}$,$Ce^{3+}$. (c) IQE, EQE, and Abs of NKLSO:$Eu^{2+}$. (d) High-resolution XRS spectra of Eu 3d before and after the post-annealing process. (e) Normalized Eu $L_3$-edge XANES spectra of $NaAlSiO_4:Eu^{2+},yLi^+$. (f) Quantity curve of $Eu^{3+}$ *versus* $Eu^{2+}$ ($I_{Eu^{2+}}/I_{Eu^{3+}}$) of $NaAlSiO_4:Eu^{2+},yLi^+$. (g) NTSC and EQE of β-SiAlON, LZAO:$Mn^{2+}$, BZAO:$Mn^{2+}$, LAO:$Mn^{2+}$, RN:$Eu^{2+}$, $N_3K_5$:$Eu^{2+}$, $R_3N$:$Eu^{2+}$, and $NK_2L$:$Eu^{2+}$. Reproduced with permission from ref. 90. Copyright 2014, Elsevier, ref. 91. Copyright 2019, Royal Society of Chemistry, ref. 26. Copyright 2023, American Chemical Society, ref. 94. Copyright 2018, American Chemical Society and ref. 95. Copyright 2019, Science.

from 70.5%/28.7% to 85.3%/40.4%.[74] Defects and oxygen vacancies induced by heterovalent substitution can reduce the QE, and so a charge compensator may be added to balance the charge. For instance, after adding the charge compensator $Al^{3+}$ to compensate for the heterovalent substitution of $Na^+$ by $Eu^{2+}$, NKLSO:$Eu^{2+}$ showed an efficient improvement in IQE/EQE values from 70%/22% to 100%/40% (Fig. 6c). $Eu^{2+}$ is a special example as rare earth (RE) ions normally exists as trivalent ions, $RE^{3+}$, hence $Eu^{2+}$-doped phosphors undergo a reduction process. The proportions of $Eu^{2+}/Eu^{3+}$ significantly decide the QE of $Eu^{2+}$-doped phosphors. A lot of methods have been reported to enhance QE and decrease the ratio of $Eu^{3+}$, such as adding reducing materials into the raw materials and using a graphite crucible or carbon paper in the sintering process.[98,99] One study reported a simple post-annealing process in a reducing $N_2/H_2$ atmosphere to reduce $Eu^{3+}$ to $Eu^{2+}$ in commercial β-SiAlON, and found the EQE was enhanced from 38.4% to 71.3%.[100] The $Eu^{2+}$ content was investigated by X-ray photoelectron spectroscopy (XPS), and it was clear that the $Eu^{2+}$ intensity was enhanced after the post-annealing process (Fig. 6d). Substitution of a cation for enhancing the QE usually changes the local environment of the lattice, which can have an effect on the activator. $NaAlSiO_4:Eu^{2+}$ showed an enhancement in the IQE from 75% to 86% by replacing $Al^{3+}$ by $Li^+$, whereby the Li atom at the Na vacancy helped reduce $Eu^{3+}$ to $Eu^{2+}$, and at same time, the incorporation of $Li^+$ changed the $Eu^{2+}$ sites and tuned the emission peak from yellow to green.[101] Eu $L_3$-edge XANES was used to directly compare the ratio of $Eu^{2+}/Eu^{3+}$, and it was observed that the $Eu^{2+}$ content increased with the increasing $Li^+$ (Fig. 6e and f). Compare the QE of the green-emitting phosphors with different activators, the $Eu^{2+}$ has the highest EQE (Fig. 6g). The highest EQE of $Eu^{2+}$ demonstrated the potential of green-emitting with good performance. The QE is not only related to the structure of phosphors, but also related to the sintering temperature and time. A long sintering time is conducive to large crystal sizes and few defects. A relatively high sintering temperature can also enhance the crystallinity and reduce the defects. A low number of defects can enhance the QE, while suitably prolonging the sintering temperature and increasing the sintering time can also enhance the QE.

## 4. Application

There are many efficient strategies to obtain narrow-band green-emitting phosphors, including combining lattice and

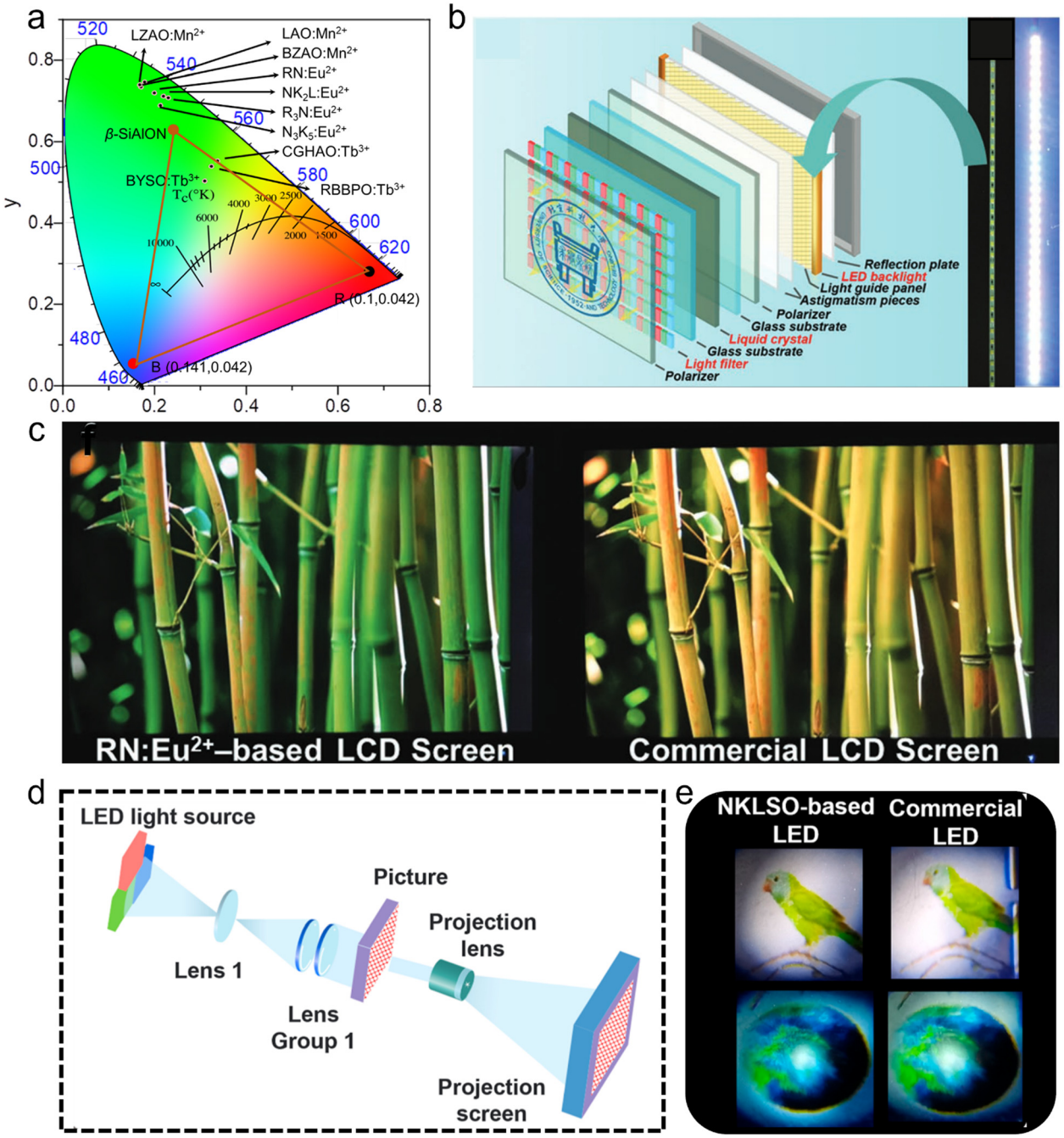


Fig. 7 (a) Color gamut of green-emitting β-SiAlON + blue chip + red-emitting KSF:$Mn^{4+}$, and the color coordinates of LZAO:$Mn^{2+}$, BZAO:$Mn^{2+}$, LAO:$Mn^{2+}$, RN:$Eu^{2+}$, $N_3K_5$:$Eu^{2+}$, $R_3N$:$Eu^{2+}$, $NK_2L$:$Eu^{2+}$, RBBPO:$Tb^{3+}$, BYSO:$Tb^{3+}$,$Ce^{3+}$, and CGHAO:$Tb^{3+}$,$Ce^{3+}$. (b) LCD prototype (left) and the backlight-1 fabricated by WLED-1 (right, blue chip + RN:$Eu^{2+}$ green-emitting and KSF:$Mn^{4+}$ red-emitting phosphors). (c) LCD screen lightened by backlight-1 (left) and backlight-2 (right, blue chip + YAG:$Ce^{3+}$ yellow-emitting and KSF:$Mn^{4+}$ red-emitting phosphors). (d) Prototype and projection mechanism of a projector. (e) Photographs of WLED-2 (left, blue chip + $N_3K_5$:$Eu^{2+}$ green-emitting and KSF:$Mn^{4+}$ red-emitting phosphors) and WLED-3 (right, blue chip + $(Sr,Ba)_2SiO_4$:$Eu^{2+}$ green-emitting and KSF:$Mn^{4+}$ red-emitting phosphors). Reproduced with permission from ref. 58. Copyright 2019, Wiley and ref. 26. Copyright 2023, American Chemical Society.

bandgap engineering with the local structure. Spectral analysis can be used to design new highly efficient green-emitting phosphors. To verify the practicality of narrow-band green-emitting phosphors, a lot of application modes are exhibited, showing the application prospect of narrow-band green-emitting phosphor.[102,103]

High-definition displays is a key focus area owing to the growing demand for such displays, where a wider color gamut could display a more colorful picture. The commercial WLEDs used for displays are fabricated by a blue chip covered by the narrow-band green-emitting β-SiAlON phosphor and red-emitting KSF:$Mn^{4+}$ phosphor, and it has color gamut of 94%

NTSC based on the color coordinates of β-SiAlON and KSF:$Mn^{4+}$, with the wide-band emission of β-SiAlON limiting the development of a wider color gamut (Fig. 7a, red triangle). The color gamuts of different doped materials was compared, including blue chip + KSF:$Mn^{4+}$ phosphor + green-emitting phosphors of LZAO:$Mn^{2+}$, BZAO:$Mn^{2+}$, LAO:$Mn^{2+}$, RN:$Eu^{2+}$, $N_3K_5$:$Eu^{2+}$, $R_3N$:$Eu^{2+}$, $NK_2L$:$Eu^{2+}$, RBBPO:$Tb^{3+}$, BYSO:$Tb^{3+}$,$Ce^{3+}$, and CGHAO:$Tb^{3+}$,$Ce^{3+}$. Their color gamuts were all extended, except for phosphors doped by $Tb^{3+}$, which also proved that $Tb^{3+}$ was not suitable as an activator in displays due to the multiple emission peaks (Fig. 7a). Narrow-band green-emitting phosphors with good performance could replace the use of β-SiAlON in novel WLEDs used for displays and extend the color gamut. The WLED-1 showed an extended color gamut to NTSC of 124%, as fabricated by blue chip + $La_{0.827}Al_{11.9}O_{19.09}$:$Mn^{2+}$ (LAO:$Mn^{2+}$) green-emitting and $K_2TiF_6$:$Mn^{4+}$ (KTF) red-emitting phosphors, which was greater than that fabricated by β-SiAlON with an NTSC of 94%.[104] Xia's group developed a LCD prototype (blue chip + RN:$Eu^{2+}$ + KSF) to verify the practicability of RN:$Eu^{2+}$, showing a more vivid picture than a commercial LCD screen (blue chip + YAG + KSF) (Fig. 7b and c).[71] NKLSO:$Eu^{2+}$ + KSF phosphors covering a blue chip were fabricated as a WLED for a projection prototype with an NTSC of 106%, exhibiting more colorful pictures than a commercial LED (blue chip + $(Sr,Ba)_2Si_2O_4$:$Eu^{2+}$ + KSF) (Fig. 7d and e).[29]

Moreover, green-emitting phosphors can also be applied in solid-state lighting with a high CRI, whereby a traditional commercial lighting device was fabricated by an n-UV chip covered by a YAG yellow-emitting phosphor.[105,106] However, the commercial WLED device had a low CRI, suggesting the color would be displayed incorrectly and it would not be healthy for the eyes. To increase the CRI, a new strategy was explored that used an n-UV chip covered by blue-, green-, and red-emitting phosphors, and full-spectrum lighting was further developed by adding extra phosphors, which could cover the gap between the blue, green, and red phosphors. A WLED exhibited a high Ra of 93.5 and color coordinates of (0.357, 0.353), and was fabricated by an n-UV chip covered by a $Sr_2Ga_2SiO_7$:1% and 5% $Eu^{2+}$ (SGSO:1% and 5% $Eu^{2+}$) yellow-green phosphor, $Ba_{0.5}Sr_{1.5}Ga_2SiO_7$:$Eu^{2+}$ (BSGSO:$Eu^{2+}$) green phosphor, and $Sr_2Si_5N_8$:$Eu^{2+}$ red phosphor.[107]

## 5. Perspectives

In this review, we summarized work on the selection of the activator and host, modulation of the luminescence, improvement of the quantum efficiency (QE), thermal stability, and application of green-emitting phosphors in recent years. Activators are typically selected from $Mn^{2+}$, $Tb^{3+}$, $Ce^{3+}$, and $Eu^{2+}$ due to their emission in the visible region. There are three methods for selection of the host, namely single-particle diagnosis, high-throughput density functional theory (DFT) calculations, and mineral-inspired prototype evolution, that may be used to directionally search for green-emitting phosphors. We discussed a variety of ways to achieve luminescence modulation, for enhancing the thermal stability and QE. Finally, multiple application modes, such as display devices and projectors, have been fabricated and exhibited wider color gamuts and more vivid pictures.

However, there is still much to improve for high-quality green-emitting phosphors in the future. The future development direction of green-emitting phosphors should be based on achieving a wider color gamut, and developing the PL intensity, QE, and thermal stability. Compared to halide perovskite phosphors, traditional inorganic oxide phosphors have certain disadvantages, such as relatively wide emission band and large particle sizes resulting from the limited solution processing, limiting their further development. Three aspects that may guide the future direction of green-emitting phosphor development are described below.

(1) The exploration of green-emitting phosphors with an aim to achieve ultra-narrow-band emission (narrower than 20 nm) together with blue light excitation, high QE, better thermal stability, and smaller particle size without the loss of QE. The enhancements to the width, QE, and thermal stability were discussed earlier in the paper and lots of approach have been explored, and more work will proceed in the foreseeable future to meet these requirements. However, a method for achieving effective smaller particle sizes is lacking, and so a future direction is to obtain small particle size green-emitting phosphors that can under solution processing for use for mini-LEDs or micro-LEDs.

(2) Another aspect is to enhance the theoretical study of the luminescence mechanism. The emission peak and width of green-emitting phosphors have been studied a lot, but specific luminescence phenomena, such as abnormal negative thermal quenching and different luminescence in similar structures, have not been analyzed in depth. Future research may pay more attention to the mechanism, electron structure correlation, and band gap in this area. Moreover, the screening of crystal databases should be promoted to select high-quality green-emitting phosphors. This would make it easier to explore new phosphors without going through a tedious human process. Not only that, theoretical calculation modules should be established that can meet the needs of customization, such as specific wavelength, bandwidth, band gap, or thermal quenching rate with increasing temperature. Researchers could then easily select the corresponding phosphors and test them by using the theoretical calculation module.

(3) The present research into green-emitting phosphors usually aims to enhance one or two properties by synthesizing new phosphors, and tends to ignore the comprehensive performance. For example, compared to the commercial β-SiAlON, research into green-emitting phosphor tends to focus on the narrower-band, but ignores the lifetime and persistent high QE after long worktime. While it is difficult to explore a perfect new phosphor, we should improve the existing phosphors by all available ways. The future development of green-emitting phosphors can be achieved by upgrading existing phosphors to enable commercial availability.

## Data availability

The authors confirm that the data supporting the findings of this study are available within the article.

## Conflicts of interest

There are no conflicts to declare.

## Acknowledgements

This work was financially supported by the National Key Research and Development Program of China (2023YFB3506600), the National Natural Science Foundation of China (NSFC No. 12374386, 12374388, 12304461, 52172166, 52072349), the Project for Science and Technology Development Plan of Jilin Province (20240101316JC).

## Notes and references

1 F. Farooq, S. Shin, J. Y. Lee, J. Kyhm, G. Kang, H. Ko and H. S. Jang, *ACS Appl. Mater. Interfaces*, 2024, **16**, 38221–38230.
2 B. Zhang, Z. Lu, H. Zhang, W. Li, J. Zhuang, C. Hu, Y. Liu, B. Lei and X. Zhang, *J. Mater. Chem. C*, 2024, **12**, 8852–8860.
3 M. Zhao, Q. Zhang and Z. Xia, *Mater. Today*, 2020, **40**, 246–265.
4 K. Han, J. Jin, X. Zhou, Y. Duan, M. V. Kovalenko and Z. Xia, *Adv. Mater.*, 2024, **36**, 2313247.
5 X. Zhou, M. Yang, C. Shen, L. Lian, L. Hou and J. Zhang, *Nano Lett.*, 2024, **24**, 3719–3726.
6 L. Yang, H. Du, J. Li, Y. Luo, X. Lin, J. Pang, Y. Liu, L. Gao, S. He, J.-W. Kang, W. Liang, H. Song, J. Luo and J. Tang, *Nat. Commun.*, 2024, **15**, 6240.
7 A. M. Srivastava, M. G. Brik, C.-G. Ma, W. W. Beers, W. E. Cohen and M. Piasecki, *J. Phys. Chem. Lett.*, 2024, **15**, 4175–4184.
8 M. Qu, S. Zhang, J. Duan, H. Dai, T. Xuan, R.-J. Xie and H. Li, *Chin. J. Lumin.*, 2024, **45**, 1399–1409.
9 Y. Zhai, D. Zhou, P. Jing, D. Li, H. Zeng and S. Qu, *J. Colloid Interface Sci.*, 2017, **497**, 165–171.
10 S. Zhang, F. Ma, J. Jiang, Z. Wang, R. T. K. Kwok, Z. Qiu, Z. Zhao, J. W. Y. Lam and B. Z. Tang, *Angew. Chem., Int. Ed.*, 2024, **63**, e202408586.
11 J. Chen, Y. Guo, B. Chen, W. Zheng, X. Zhang, X. Wei, Y. Cao, H. Suo and F. Wang, *Adv. Opt. Mater.*, 2024, **12**, 2400147.
12 G. H. Lee, K. Kim, Y. Kim, J. Yang and M. K. Choi, *Nano-Micro Lett.*, 2023, **16**, 45.
13 X. Yu, X. Yang, H. Zhang, K. Liu and J. Yu, *Matter*, 2024, **7**, 2490–2506.
14 C. Liu, C. Wei, X. Luo, Z. Sun, B. Xu and H. Zeng, *Chin. J. Lumin.*, 2024, **45**, 1410–1430.
15 T. Xuan, S. Guo, W. Bai, T. Zhou, L. Wang and R.-J. Xie, *Nano Energy*, 2022, **95**, 107003.
16 Y. Lu, Y. Xu, S. Chen, J. Lin, J. Zhu, S. Wang, Y. Zheng, F. Huang and D. Chen, *J. Lumin.*, 2022, **248**, 118952.
17 W. Niu, X. Xie, Z. Chen, R. Sun, Y. Li, S. Wang, Y. Zhang, C. Yang and A. Tang, *Adv. Opt. Mater.*, 2024, **12**, 2400762.
18 X. He, T. Li, Z. Liang, R. Liu, X. Ran, X. Wang, L. Guo and C. Pan, *Adv. Opt. Mater.*, 2024, **12**, 2302726.
19 S. Liu, L. Li, X. Qin, R. Du, Y. Sun, S. Xie, J. Wang, M. S. Molokeev, S. Xi, J.-C. G. Bünzli, L. Zhou and M. Wu, *Adv. Mater.*, 2024, **36**, 2406164.
20 M.-H. Fang, J. L. Leaño and R.-S. Liu, *ACS Energy Lett.*, 2018, **3**, 2573–2586.
21 S. Gai, P. Gao, K. Chen, C. Tang, Y. Zhao, J. Wei, Y. Zhang, M. S. Molokeev, M. Xia and Z. Zhou, *Adv. Opt. Mater.*, 2024, **12**, 2302870.
22 Z. Xu, Z. Zhang, H. Sun and Q. Zhang, *J. Chin. Soc. Rare Earths*, 2024, **42**, 901–908.
23 S. A. Khan, N. Z. Khan, Y. Xie, M. Rauf, I. Mehmood, J. Ahmed, S. M. Alshehri, M. A. M. Khan, J. Zhu and S. Agathopoulos, *J. Lumin.*, 2022, **243**, 118650.
24 Y. Zhu, Y. Liang, S. Liu, H. Li and J. Chen, *Adv. Opt. Mater.*, 2019, **7**, 1801419.
25 Q. Liu, P. Dang, G. Zhang, H. Lian, Z. Cheng, G. Li and J. Lin, *Chem. Mater.*, 2024, **36**, 1763–1772.
26 V. Rajagopal, R.-J. Xie and R. Nagaraj, *J. Lumin.*, 2022, **252**, 119356.
27 S. Wang, H. Wu, Y. Fan, Q. Wang, T. Tan, R. Pang, S. Zhang, D. Li, L. Jiang, C. Li and H. Zhang, *Chem. Eng. J.*, 2022, **432**, 134265.
28 L. Zheng, L. Zhang, L. Fang, H. Wu, H. Wu, G.-H. Pan, Y. Yang, Y. Luo, Z. Hao and J. Zhang, *Adv. Opt. Mater.*, 2024, **12**, 2301480.
29 Y. Wan, P. Dang, D. Liu, Q. Zhang, Y. Wei, H. Lian, G. Li and J. Lin, *Chem. Mater.*, 2023, **35**, 10702–10712.
30 S. Li, R. Tian, T. Yan, Y. Guo, Y. Liu, T.-L. Zhou, L. Wang and R.-J. Xie, *Mater. Today*, 2023, **70**, 82–92.
31 K. Zhang, W. Fan, T. Yao, S. Wang, Z. Yang, J. Yao, L. Xu and J. Song, *Adv. Mater.*, 2024, **36**, 2310521.
32 Z. Li, N. Yang, S. Ding, Z. Zhang, W. Huang, Z. Ye, M. Zhao and J. Shi, *J. Mater. Sci. Technol.*, 2025, **205**, 159–167.
33 S.-Y. Zhu, D. Zhao, S.-J. Dai, R.-J. Zhang and L.-Y. Shi, *CrystEngComm*, 2022, **24**, 2966–2975.
34 X. Zhu, S. Zhang and S. Ye, *J. Phys. Chem. Lett.*, 2024, **15**, 2804–2814.
35 S. Li, W. Hu, M. G. Brik, S. Lian and Z. Qiu, *Inorg. Chem. Front.*, 2022, **9**, 3224–3232.
36 E. H. Song, Y. Y. Zhou, Y. Wei, X. X. Han, Z. R. Tao, R. L. Qiu, Z. G. Xia and Q. Y. Zhang, *J. Mater. Chem. C*, 2019, **7**, 8192–8198.
37 X. Zhu, S. Zhang and S. Ye, *J. Phys. Chem. Lett.*, 2024, **15**, 2804–2814.
38 P. Dang, H. Lian and J. Lin, *Adv. Opt. Mater.*, 2023, **11**, 2202511.
39 W. Wang, H. Yang, M. Fu, X. Zhang, M. Guan, Y. Wei, C. C. Lin and G. Li, *Chem. Eng. J.*, 2021, **415**, 128979.
40 H. R. Girisha, B. R. Radha Krushna, K. Manjunatha, H.-H. Chiu, M.-K. Ho, S. Y. Wu, B. Subramanian and

 

H. Nagabhushana, *Mater. Today Sustainability*, 2023, **24**, 100493.
41 X. Liu, H. Cheng, B. Yue, Z. Wen, Y. Jin, G. Liu, S. Liu, D. Li, J. Wang, W. Yu and X. Dong, *J. Colloid Interface Sci.*, 2024, **666**, 162–175.
42 B. C. Jamalaiah, P. S. Khan, N. Madhu, P. Gawas, V. Nutalapati, A. S. Narayana Reddy and G. V. L. Reddy, *Ceram. Int.*, 2022, **48**, 28927–28934.
43 H. Zhang, Q. Ding, F. Chen, Y. Miao, D. Yu and D. Zhang, *Chin. J. Lumin.*, 2024, **45**, 1114–1122.
44 J. Chang, Y. Wang, Z. Zhang, D. Guo, P. Zhao, N. Wang, Z. Wang, L. Li, P. Li and H. Suo, *Laser Photonics Rev.*, 2023, **17**, 2300542.
45 G. W. Jung and K. Park, *J. Mater. Sci. Technol.*, 2021, **82**, 187–196.
46 Y. Chen, J. Wang, X. Zhang, G. Zhang, M. Gong and Q. Su, *Sens. Actuators, B*, 2010, **148**, 259–263.
47 S. Yang, W. Sun, Q. Xu, C. Yang, S. Zhang and M. Jiao, *Spectrochim. Acta, Part A*, 2023, **292**, 122402.
48 Z. Huang, Z. Lyu, S. Shen, S. Wang, Z. Yang, C. Chen and H. You, *Inorg. Chem.*, 2024, **63**, 6362–6369.
49 X. Huang, J. Liang, S. Rtimi, B. Devakumar and Z. Zhang, *Chem. Eng. J.*, 2021, **405**, 126950.
50 J. Liang, L. Sun, S. Wang, Q. Sun, B. Devakumar and X. Huang, *J. Alloys Compd.*, 2020, **836**, 155469.
51 Y. Xiao, Z. Hao, L. Zhang, X. Zhang, G.-H. Pan, H. Wu, H. Wu, Y. Luo and J. Zhang, *J. Mater. Chem. C*, 2018, **6**, 5984–5991.
52 Y. Lin, H. Lin, P. Wang, J. Xu, Y. Cheng and Y. Wang, *Laser Photonics Rev.*, 2024, 2400995, DOI: **10.1002/lpor.202400995**.
53 Y. Guo, Y. Wang, Y. Lu, L. Luo, W. Li and P. Du, *Laser Photonics Rev.*, 2024, 2400183, DOI: **10.1002/lpor.202400183**.
54 Y. Du, T. Seto, W. Liu, Y. Wang and X. Ma, *Adv. Opt. Mater.*, 2024, **12**, 2302183.
55 B. Guo, M. Wen, H. Tang, S. Lishik, X. Fan, G. Zhang and J. Fan, *Laser Photonics Rev.*, 2024, **18**, 2300838.
56 S. Tian, P. Fen, X. Qiao and Y. Wang, *J. Chin. Soc. Rare Earths*, 2024, **42**, 894–900.
57 X. Luo and R.-J. Xie, *J. Rare Earths*, 2020, **38**, 464–473.
58 R. Lu and J. Sun, *Materials*, 2023, **16**, 5053.
59 Z. Xia, Z. Xu, M. Chen and Q. Liu, *Dalton Trans.*, 2016, **45**, 11214–11232.
60 T. Takeda, N. Hirosaki, S. Funahashi and R.-J. Xie, *Mater. Discovery*, 2015, **1**, 29–37.
61 T. Takeda, N. Hirosaki, S. Funahshi and R.-J. Xie, *Chem. Mater.*, 2015, **27**, 5892–5898.
62 H. Ming, Y. Zhou, M. S. Molokeev, C. Zhang, L. Huang, Y. Wang, H.-T. Sun, E. Song and Q. Zhang, *ACS Mater. Lett.*, 2024, **6**, 1790–1800.
63 M. Liao, Z. Mu, Q. Wang, X. Zhang, H. Dong, M. Wen and F. Wu, *J. Alloys Compd.*, 2020, **837**, 155084.
64 C. Park, J.-W. Lee, M. Kim, B. D. Lee, S. P. Singh, W. B. Park and K.-S. Sohn, *Inorg. Chem. Front.*, 2021, **8**, 4610–4624.
65 R. Shafei, D. Maganas, P. J. Strobel, P. J. Schmidt, W. Schnick and F. Neese, *J. Am. Chem. Soc.*, 2022, **144**, 8038–8053.
66 J. Brgoch, S. P. DenBaars and R. Seshadri, *J. Phys. Chem. C*, 2013, **117**, 17955–17959.
67 Q. Zhang, X. Ding, H. Wang, B. Liu and Y. Wang, *J. Mater. Chem. C*, 2023, **11**, 15366–15375.
68 J. Sun, W. Zhu, B. Zhang, F. Huang, L. Hu, H. Ma, R. Ye, Y. Hua and S. Xu, *Opt. Mater.*, 2023, **146**, 114529.
69 F. Ruegenberg, A. García-Fuente, M. Seibald, D. Baumann, G. Hoerder, T. Fiedler, W. Urland, H. Huppertz, A. Meijerink and M. Suta, *Adv. Opt. Mater.*, 2023, **11**, 2202732.
70 J. Sun, M. Zhou, B. Zhang, Y. Hua, F. Huang, H. Ma, R. Ye and S. Xu, *Dalton Trans.*, 2022, **51**, 11703–11712.
71 H. Liao, M. Zhao, Y. Zhou, M. S. Molokeev, Q. Liu, Q. Zhang and Z. Xia, *Adv. Funct. Mater.*, 2019, **29**, 1901988.
72 X. Wang, X. Huang, M. Zhao, P. A. Tanner, X. Zhou and L. Ning, *Inorg. Chem.*, 2022, **61**, 7617–7623.
73 M. Zhao, H. Liao, L. Ning, Q. Zhang, Q. Liu and Z. Xia, *Adv. Mater.*, 2018, **30**, 1802489.
74 M. Liao, Q. Wang, Q. Lin, M. Xiong, X. Zhang, H. Dong, Z. Lin, M. Wen, D. Zhu, Z. Mu and F. Wu, *Adv. Opt. Mater.*, 2021, **9**, 2100465.
75 M.-H. Fang, C. O. M. Mariano, K.-C. Chen, J.-C. Lin, Z. Bao, S. Mahlik, T. Lesniewski, K.-M. Lu, Y.-R. Lu, Y.-J. Wu, H.-S. Sheu, J.-F. Lee, S.-F. Hu, R.-S. Liu and J. P. Attfield, *Chem. Mater.*, 2021, **33**, 1893–1899.
76 M. Liao, F. Wu, J. Wang, D. Zhu, X. Zhang, H. Dong, Z. Lin, M. Wen and Z. Mu, *ACS Appl. Mater. Interfaces*, 2022, **14**, 47892–47901.
77 J. Xu, C. He, L. Zeng, G. Li, C. Li, H. Lin, J. Liu, L. Zhou, J. Yang and J. Tang, *J. Lumin.*, 2024, **268**, 120398.
78 T. Giftthaler, P. Strobel, V. Weiler, A. Haffner, A. Neuer, J. Steinadler, T. Bräuniger, S. D. Kloß, S. Rudel, P. J. Schmidt and W. Schnick, *Adv. Opt. Mater.*, 2024, **12**, 2302343.
79 J. Qiao, Y. Zhou, M. S. Molokeev, Q. Zhang and Z. Xia, *Laser Photonics Rev.*, 2021, **15**, 2100392.
80 Y. Zhuo, S. Hariyani, J. Zhong and J. Brgoch, *Chem. Mater.*, 2021, **33**, 3304–3311.
81 H. Zhang, H. Li, C. Liu, H. Jiang, J. Li, Y. Liu, J. He, R. Wang, W. Hu and J. Zhu, *Chem. Eng. J.*, 2024, **490**, 151727.
82 D. Wen, H. Liu, Z. Ma, L. Zhou, J. Li, Y. Guo, Q. Zeng, P. A. Tanner and M. Wu, *Angew. Chem., Int. Ed.*, 2023, **62**, e202307868.
83 S. Hariyani, A. C. Duke, T. Krauskopf, W. G. Zeier and J. Brgoch, *Appl. Phys. Lett.*, 2020, **116**, 051901.
84 R. Shi, S. Cao, Y. Han, J. Zhang, X. Zhang, S. Liao and S. Lian, *Appl. Mater. Today*, 2022, **29**, 101625.
85 R. Shi, X. Zhang, Z. Qiu, J. Zhang, S. Liao, W. Zhou, X. Xu, L. Yu and S. Lian, *Inorg. Chem.*, 2021, **60**, 19393–19401.
86 M. Zhao, K. Cao, M. Liu, J. Zhang, R. Chen, Q. Zhang and Z. Xia, *Angew. Chem., Int. Ed.*, 2020, **59**, 12938–12943.
87 G. Liu, W. Chen, Z. Xiong, Y. Wang, S. Zhang and Z. Xia, *Nat. Photonics*, 2024, **18**, 562–568.
88 S. Li, Y. Guo and R.-J. Xie, *Acc. Mater. Res.*, 2022, **3**, 1299–1308.
89 S. Li, L. Wang, N. Hirosaki and R.-J. Xie, *Laser Photonics Rev.*, 2018, **12**, 1800173.

90 B. Zhang, J. Zhou, W. Zhu, F. Huang, R. Ye, H. Ma, Y. Hua and S. Xu, *Ceram. Int.*, 2024, **50**, 5868–5876.
91 Y. Zhou, C. Li, J. Ning and F. Tang, *Adv. Opt. Mater.*, 2024, **12**, 2400374.
92 Z. Zhang, Y. Ren, S. Zhang, H. Mu, X. Li and X. Sun, *J. Chin. Soc. Rare Earths*, 2024, **42**, 909–917.
93 Z. Lu, D. Sun, Z. Lyu, S. Shen, X. Zhang, S. Wei, P. Luo, L. Zhou and H. You, *Mater. Today Chem.*, 2023, **34**, 101813.
94 W. Ahn, M. Im and Y. J. Kim, *Mater. Res. Bull.*, 2017, **96**, 254–257.
95 J. Gao, L. Dong, Y. Lin, P. Zhou, X. Ma, J. Hou and Y. Fang, *J. Mater. Chem. C*, 2024, **12**, 7435–7445.
96 Y. Yu, H. Wang, L. Li, Y. Chen and R. Zeng, *Ceram. Int.*, 2014, **40**, 14171–14175.
97 L. Sun, B. Devakumar, J. Liang, S. Wang, Q. Sun and X. Huang, *J. Mater. Chem. C*, 2019, **7**, 10471–10480.
98 Z. Yang, G. Liu, Y. Zhao, Y. Zhou, J. Qiao, M. S. Molokeev, H. C. Swart and Z. Xia, *Adv. Opt. Mater.*, 2022, **10**, 2102373.
99 J. Qiao, S. Zhang, X. Zhou, W. Chen, R. Gautier and Z. Xia, *Adv. Mater.*, 2022, **34**, 2201887.
100 S. Li, L. Wang, D. Tang, Y. Cho, X. Liu, X. Zhou, L. Lu, L. Zhang, T. Takeda, N. Hirosaki and R.-J. Xie, *Chem. Mater.*, 2018, **30**, 494–505.
101 M. Zhao, Z. Xia, X. Huang, L. Ning, R. Gautier, M. S. Molokeev, Y. Zhou, Y.-C. Chuang, Q. Zhang, Q. Liu and K. R. Poeppelmeier, *Sci. Adv.*, 2019, **5**, eaav0363.
102 R.-J. Xie, N. Hirosaki and T. Takeda, *Appl. Phys. Express*, 2009, **2**, 022401.
103 X. Li, W. Feng, F. You, T. Pang, J. Zhu, J. Lin, Y. Fang and D. Chen, *Adv. Opt. Mater.*, 2023, 2302823.
104 C. Zhan, H. Zhu, S. Liang, Y. Huang, Z. Wang and M. Hong, *Inorg. Chem. Front.*, 2024, **11**, 826–836.
105 W. Xia, Q. Zhao, L. Du, F. Du, Y. Zhang, T. Zhang, F. Hao and Z. Tang, *Chem. Eng. J.*, 2024, **484**, 149723.
106 P. He, Y. Li, J. Zuo, B. Zhang, F. Yang, J. Peng, S. Liu, W. Wang, D. Huang, Y. Xiao and X. Ye, *J. Alloys Compd.*, 2024, **985**, 173997.
107 D. Liu, R. Zhao, C. Wang, Z. Liu, J. Zhang, Y. Wang, X. Yu, J. Qiu, X. Xu and Y. Liu, *Mater. Today Phys.*, 2024, **40**, 101325.

 